
Article:
Synnott, F.E., Owen, L.R., Jones, N.G. et al. (2026) In situ X-ray characterization of thermomechanical deformation behavior in powder-processed polycrystalline high co-containing Ni-based superalloys. Metallurgical and Materials Transactions A. ISSN: 1073-5623

https://doi.org/10.1007/s11661-026-08142-x

In Situ X-ray Characterization of Thermomechanical Deformation Behavior in Powder-Processed Polycrystalline High Co-Containing Ni-Based Superalloys

FRANCES E. SYNNOTT, LEWIS R. OWEN, NICHOLAS G. JONES, HOWARD J. STONE, DAVID DYE, PAUL M. MIGNANELLI, MARK HARDY, and KATERINA A. CHRISTOFIDOU

Polycrystalline Ni-based superalloys rely on compositional modifications for high-temperature, structural aerospace applications. However, these changes must be carefully managed to avoid deleterious phases. While the individual effects of Ti and Ta are well documented, their synergistic co-addition has received limited attention in high Co-containing alloys. This study investigates the influence of Ti and Ta on the load partitioning behavior between the γ and γ' phases using *in situ* synchrotron diffraction under tensile loads in the temperature range from 600 °C to 800 °C. Our findings show that the ratio of Ti:Ta directly impacts how load is distributed, with a higher ratio leading to a greater load-carrying capacity in the γ' phase, thereby improving strength at intermediate temperatures (700 °C). However, this benefit seems thermally limited, coinciding with a significant reduction in stiffness in the high-Ti alloy at 800 °C. Conversely, a balanced Ti:Ta ratio maintains consistent load partitioning and strength stability across the entire temperature range. By linking lattice misfit and stiffness evolution to bulk behavior, this work identifies load transfer efficiency as a critical metric for the design of future high-performance superalloys. By understanding this relationship, the compositional limits for optimizing alloy performance in service can be better defined. This work highlights a critical design pathway for future high-performance superalloys by demonstrating the link between controlled alloying, lattice misfit, and load partitioning.

https://doi.org/10.1007/s11661-026-08142-x

I. INTRODUCTION

Ni-based superalloys are the material of choice for demanding aerospace applications. Their remarkable strength is derived from a two-phase microstructure, consisting of a γ matrix and a high-volume fraction of coherent, ordered γ' precipitates. The mechanical behavior of these alloys is not solely dependent on the bulk properties, but on how the load is partitioned between the softer γ matrix and the primary strengthening γ' phase. Therefore, understanding the load partitioning behavior between the two phases is essential for the design of next-generation alloys.

Previous studies have demonstrated that the γ' phase often carries a disproportionate amount of the load, especially at room temperature, while the load sharing changes as temperature increases, with the phases having similar moduli at elevated temperatures.[1] This dynamic load distribution is critical to the alloy's performance and is influenced by both the initial microstructure and ongoing plastic deformation.[2, 3]

FRANCES E. SYNNOTT is with the Aerospace Technology Institute, Martell House, University Way, Cranfield MK43 0TR, UK and also with the School of Chemical, Materials and Biological Engineering, The University of Sheffield, Sir Robert Hadfield Building, Mappin Street, Sheffield S1 3JD, UK. LEWIS R. OWEN and KATERINA A. CHRISTOFIDOU are with the School of Chemical, Materials and Biological Engineering, The University of Sheffield. Contact e-mail: k.christofidou@sheffield.ac.uk NICHOLAS G. JONES and HOWARD J. STONE are with the Department of Materials Science and Metallurgy, The University of Cambridge, Charles Babbage Road, Cambridge CB3 0FS, UK. DAVID DYE is with the Department of Materials, Imperial College London, South Kensington Campus, London SW7 2AZ, UK. PAUL M. MIGNANELLI and MARK HARDY are with the Rolls-Royce plc., PO Box 31, Derby DE24 8BJ, UK.

Manuscript submitted September 30, 2025; accepted January 27, 2026.

Published online: 16 February 2026

Titanium and tantalum are crucial alloying elements, known for their ability to modify the microstructure and properties of superalloys. Both Ti and Ta are strong γ'-formers, increasing the γ' solvus temperature, promoting stability at higher temperatures, and increasing the antiphase boundary energy. In addition, Ta can also provide significant solid-solution strengthening to the γ phase as well.[4–7] Furthermore, high cobalt-containing alloys are of particular interest due to a change in elemental partitioning that can enable a reduction in deleterious phase formation and improvements in performance.[8–12] However, a particular gap exists in our understanding of how these co-additions, in the presence of high Co concentrations, influence the load partitioning between the γ and γ' phases under tensile loads, a critical factor in understanding how these alloys operate in service.

In polycrystalline materials, stress manifests across multiple scales, with anisotropic elastic behavior arising from differences in grain orientation and varying critical resolved shear stress (CRSS) among different grain families. In high γ' fraction alloys, tensile interphase stresses are known to form in the stronger γ' phase in {100} grains, while compressive stresses occur in {110} grains, with the inverse occurring in the γ matrix.[13] At low applied stress, resolving phase-specific behavior is challenging due to the similar lattice parameters of γ and γ', which results in difficulties in unambiguously differentiating between the diffraction peaks of the two phases.[14] However, as stress increases and plastic deformation initiates, strain-induced peak broadening and asymmetry enable a clearer phase distinction and reveal the load transfer between phases.[15, 16] A detailed understanding of these phenomena is essential for predicting the onset of plastic deformation and subsequent failure.

Consequently, this study uses *in situ* synchrotron X-ray diffraction to directly measure the evolution of lattice strains and the resulting load partitioning between the γ and γ' phases as a function of temperature up to 800 °C. By systematically varying the Ti:Ta ratio, this study aims to establish a direct link between alloy composition, lattice misfit, and the load partitioning behavior between the γ and γ' phases. This work allows for the compositional optimization of high-performance superalloys by understanding the limits of alloying in service.

II. EXPERIMENTAL METHODS

Alloys A–C were manufactured with varying Ti:Ta content to evaluate the co-additions of Ta and Ti.[17, 18] The sum of Ti and Ta was kept at a constant of 6 at. pct to achieve similar γ' volume fractions, with the remaining element concentrations kept constant. Table I lists the nominal and actual compositions for Alloys A–C. The actual compositions were measured using inductively coupled plasma-optical emission spectrometry (ICP-OES), glow discharge, and combustion analysis. All alloys were gas atomized, encapsulated in cylindrical steel cans each measuring approximately 2.5 cm in diameter and 12 cm in length, and subjected to hot isostatic pressing (HIP) at 1107 °C and 100 MPa for 4 hours. The consolidated ingots were homogenized at 1200 °C for 2 hours, then aged at 850 °C for 4 hours, followed by bench cooling after each step.

Microstructural analysis was conducted using secondary electron (SE) imaging mode on a JEOL JSM-7900F scanning electron microscope (SEM) operated at 20 kV. Additionally, electron backscatter diffraction (EBSD) was performed using the Oxford Instruments Aztec HKL Advanced Symmetry EBSD system, with subsequent grain structure analysis conducted using MTEX. For γ' precipitate analysis, the samples were electrolytically etched using a 10 pct phosphoric acid solution at 3 V. All microscopy samples were polished to a 0.04 μm colloidal silica finish and ultrasonically cleaned in isopropanol prior to imaging. The area fraction of γ' and MC phases was measured using the Trainable Weka Segmentation tool in Fiji, where the SEM images were segmented into a 5×5 matrix, and the area fraction calculated for each segment. The results were then averaged, with the standard deviation reported as the error. Grain size and γ' precipitate size are reported as equivalent circular diameters (ECDs).

A series of *in situ* tensile tests was conducted on the ID15B beamline at the European Synchrotron Radiation Facility (ESRF) to investigate the mechanical behavior of these alloys in their aged state and, more importantly, to elucidate the temperature dependence of γ/γ' load partitioning. An Instron electro-thermal mechanical testing (ETMT) instrument was used at the ESRF and tensile bow-tie specimens were prepared using electro-discharge machining (EDM) with a gauge volume of 1.5 mm × 1.5 mm × 12 mm. Tensile testing was conducted at 600 °C, 700 °C, and 800 °C using a tensile strain rate of 10^{-3} s^{-1}.

2D powder diffraction patterns were collected on a Pixium detector every 0.5 seconds at an energy of 87.3 keV, equating to a wavelength of 0.142 Å. Patterns of pure ceria were also collected and used to calibrate the wavelength and sample-to-detector distances. The raw 2D diffraction data were divided into 10 deg segments and azimuthally integrated using GSAS-II with an angular 2θ range of 2.25 to 10.5 deg, azimuth angle of 85 to 95 deg, and binning number of 800. The specific lattice reflections presented in the results section were selected based on the quality of the diffraction peaks and the resultant statistical reliability of the peak fits. Due to the interaction between the beam gauge volume and the alloy grain size (approx. 30 to 38 μm), certain reflections exhibited variations in peak intensity or symmetry (grain statistics) that precluded accurate lattice strain analysis. Consequently, reflections were chosen to maximize the signal-to-noise ratio for each composition. Pawley refinements were also completed using GSAS-II to measure the γ and γ' lattice parameters and subsequently derive the γ/γ' lattice misfit.

To derive the d spacing for each phase for a given reflection, single peak fits of the γ and γ' peaks using a Pseudo-Voigt peak profile were conducted sequentially using the Line-Profile Analysis Software (LIPRAS)

Table I. Nominal and Actual Chemical Compositions of Alloys A–C and Actual Compositions (At. Pct) Measured using ICP-OES, Glow Discharge, and Combustion Analysis[17, 18]

Alloy	Composition (At. Pct)											
	Ni	Co	Cr	Ti	Al	Ta	Mo	W	B	C	Zr	Ti:Ta
A												
Nominal	bal.	26.00	15.50	3.60	6.40	2.40	1.50	0.50	0.15	0.15	0.03	1.50
Actual	bal.	25.60	14.90	3.42	5.89	2.40	1.53	0.50	0.14	0.14	0.03	1.43
B												
Nominal	bal.	26.00	15.50	4.20	6.40	1.80	1.50	0.50	0.15	0.15	0.03	2.30
Actual	bal.	26.00	15.30	3.97	6.23	1.82	1.55	0.48	0.16	0.12	0.03	2.18
C												
Nominal	bal.	26.00	15.50	5.40	6.40	0.60	1.50	0.50	0.15	0.15	0.03	9.00
Actual	bal.	26.00	15.00	5.18	5.96	0.69	1.54	0.50	0.17	0.14	0.04	7.51

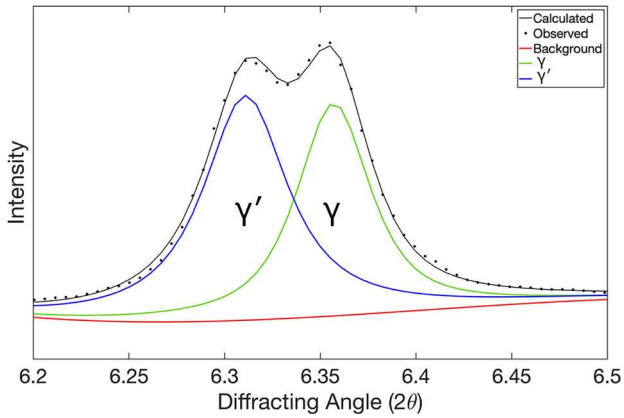

Fig. 1—Single peak fitting of the {220} peak in Alloy B at 800 °C using LIPRAS.

package within MATLAB.[19] An example of a typical fit is shown in Figure 1. Due to the similarities in lattice parameters and thus peak positions between the γ and γ' phases, an additional constraint on the peak intensity ratio, N, was implemented in the fits to retain physically meaningful results. The peak intensity ratio N, Eq. [1], was derived from the relative phase volume fractions ($\gamma_{vf}, \gamma'_{vf}$) and form factor calculations (f) of each phase. These parameters were obtained using data from thermodynamic modeling to account for phase composition and lattice site occupancy in both the γ and γ' phases.[2, 13, 16, 20, 21]

$$N = \frac{\gamma_{vf} \times [4 \times f_{\text{total}}]^2}{\gamma'_{vf} \times [(3 \times f_{\text{face}}) + f_{\text{corner}})]^2} \quad [1]$$

Table II summarizes the calculated γ' volume fractions using Thermo-Calc with the TCNI8 database, along with the derived N constraint used in the fitting functions.

Following derivation of the d-spacing, the lattice strain (ε_{hkl}) was calculated using Eq. [2], where $d_{0,hkl}$ is the initial d-spacing value for a peak at the beginning of testing, when no stress is applied, and d_{hkl} is the d-spacing value for a peak at a given applied stress.

Table II. γ' Volume Fraction and Integrated Intensity Constraint, N, for Alloys A–C Obtained from Thermo-Calc TCNI8 Database for Fundamental γ-γ' Peaks

Alloy	Temperature (°C)	γ' Volume Fraction (Pct)	N
A	600	50.8	0.903
	700	48.5	1.011
	800	43.7	1.251
B	600	50.9	0.957
	700	48.8	1.049
	800	44.2	1.286
C	600	51.1	1.042
	700	49.2	1.132
	800	46.2	1.279

Errors on the derived strains were obtained using the propagation of errors based on the d-spacing error on each peak and reflection.

$$\varepsilon^{\gamma}_{hkl} = \frac{d^{\gamma}_{hkl} - d^{\gamma}_{0,hkl}}{d^{\gamma}_{0,hkl}} \; and \; \varepsilon^{\gamma'}_{hkl} = \frac{d^{\gamma'}_{hkl} - d^{\gamma'}_{0,hkl}}{d^{\gamma'}_{0,hkl}} \quad [2]$$

To further quantify the effects of Ti and Ta co-additions, the anti-phase boundary energies (APBEs) of Alloys A–C were calculated using the TCNI12 database in Thermo-Calc 2024b. Calculations were performed using the Anti-phase Boundary Property Model Calculator and actual alloy compositions, for the {111} and {100} planes as well as the average surface energy. The APBE interface within Thermo-Calc implements the methods outlined in a number of publications.[22–25]

III. RESULTS

The microstructure of the three alloys was characterized in the aged condition using EBSD and SEM to provide context for the mechanical performance. EBSD measurements revealed that the alloys possess comparable grain structures, with mean grain Equivalent Circular Diameters (ECDs) of 34.5 ± 22.1 μm for Alloy

A, 30.45 ± 25.9 μm for Alloy B, and 38.2 ± 20.4 μm for Alloy C. Analysis of SEM micrographs shown in Figure 2 confirmed the presence of a multimodal precipitate distribution. The volume fractions of the secondary γ' precipitates were determined to be 48.5 ± 4.1, 50.5 ± 4.6, and 53.6 ± 5.0 pct for Alloys A, B, and C, respectively. Additionally, a population of finer tertiary precipitates was observed, with measured volume fractions of 3.2 ± 1.4 pct (Alloy A), 4.4 ± 1.5 pct (Alloy B), and 6.1 ± 2.2 pct (Alloy C). The thermodynamic predictions presented in Table II were compared against the experimentally determined phase fractions. While the absolute values differ slightly, the general trends are entirely consistent. The measured total γ' volume fraction increased systematically across the cohort (Alloy A < Alloy B < Alloy C), confirming the computational prediction that the higher Ti concentration (relative to Ta) in Alloy C promotes a larger γ' volume fraction. In addition to the γ' volume fractions, the size distributions were also quantified. The mean ECDs of the secondary precipitates were consistent across the compositions, measuring 416 ± 143 nm, 407 ± 120 nm, and 423 ± 164 nm for Alloys A through C, respectively. The tertiary precipitates were significantly finer, with mean ECDs of 55.0 ± 44.2 nm, 53.5 ± 34.7 nm, and 70.5 ± 38.2 nm, respectively.

The yield strength and bulk elastic modulus of the three alloys were measured using ETMT tensile testing in the temperature range of 600 °C to 800 °C (see electronic supplementary Figure S1). However, due to both the miniaturization of the samples and the nature of ETMT testing, only the elastic region is considered reliable, and thus, no quantitative results are presented herein for UTS or ductility. Figure 3 demonstrates a lack of a simple correlation between temperature, yield strength, and alloy composition. Alloy A, with the lowest Ti:Ta ratio, shows the highest relative strength at 600 °C, but this declines significantly at 700 °C and 800 °C to near identical values of 600 MPa and 595 MPa, respectively. In contrast, Alloy B exhibits a more consistent strength across all temperatures, while Alloy C (highest Ti:Ta ratio) shows a marginally higher strength at 700 °C but a sharp decline at 800 °C.

An analysis of the lattice misfit, determined from Pawley refinement of the diffraction patterns, is presented in Figure 4. At room temperature, the lattice misfit is relatively high for Alloys A and B, 0.614 and 0.506 pct, respectively, whereas for Alloy C, the lattice misfit is significantly lower at 0.145 pct. At higher temperatures, a sharp decrease is observed in the misfit of both Alloys A and B, whereas for Alloy C, misfit remains within a narrow, stable range of 0.122 to 0.160 pct. With the exception of 800 °C, the lattice misfit for Alloy A is consistently higher than either Alloy B or C. Interestingly, in the temperature range of 600 °C to 800 °C, the lattice misfit between alloys B and C exhibits significant overlap.

The *in situ* diffraction data provide a detailed view of how load is partitioned between the γ and γ' phases. To better understand the relationships between composition, temperature, and orientation, the results are presented in three distinct categories. Representative examples are shown across each section, and the full data can be found in the open repository indicated. A numerical (Table S1) and graphical summary of the

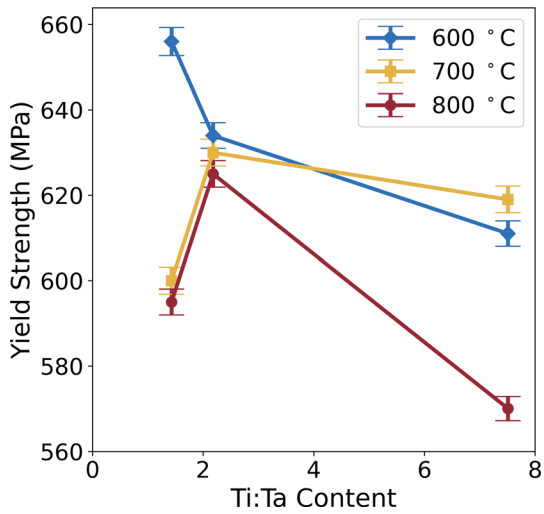

Fig. 3—The bulk yield strength for Alloys A (Ti:Ta = 1.43), B (Ti:Ta = 2.18), and C (Ti:Ta = 7.51), measured at 600 °C to 800 °C from ETMT.

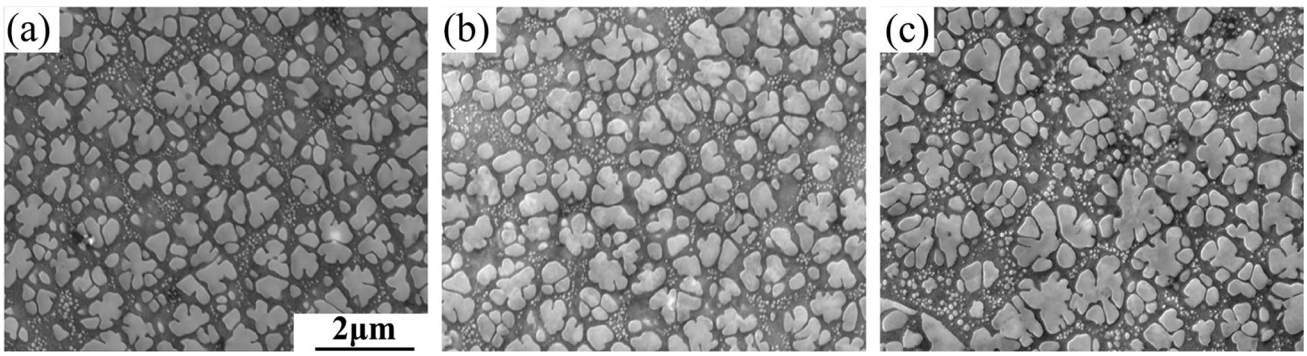

Fig. 2—SEM images of alloys in the aged condition (1200 °C/2 h + 850 °C/4 h): (*a*) Alloy A, (*b*) Alloy B, and (*c*) Alloy C, showing a multimodal γ' microstructure.

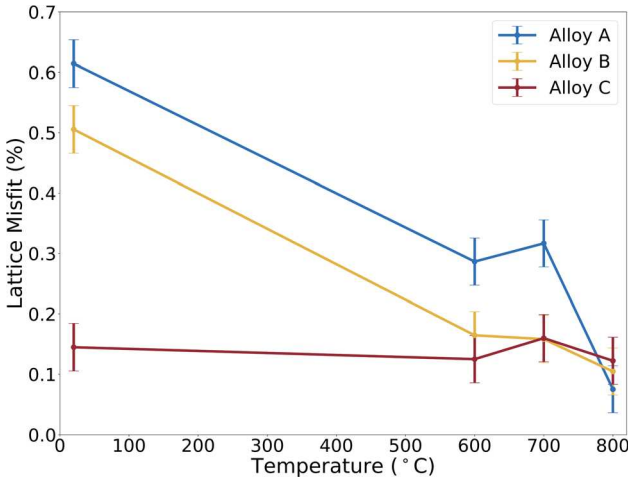

Fig. 4—The lattice misfit of Alloys A–C unstressed, at room temperature, and 600 °C–800 °C.

yield strength and diffraction elastic moduli (Figures S2-3) is provided in the electronic supplementary. First, the effect of orientation for a given alloy at a specific temperature is presented, Figure 5. Second, the effect of temperature for a given crystallographic orientation and specific alloy composition is examined, Figure 6. Finally, the effect of composition is explored by contrasting the load partitioning behavior between the three alloys at a given temperature and for a specific orientation, Figure 7.

IV. EFFECTS OF ORIENTATION

A. *Alloy A at 700 °C*

The load partitioning behavior of Alloy A at 700 °C is highly dependent on crystallographic orientation, as shown in Figures 5(a) through (c). Across all reflections studied, the γ phase consistently exhibits a higher elastic modulus (stiffness) than the γ' phase, with {311} as an exception. In the {200} reflection, both phases yield below 600 MPa, a value close to the bulk yield strength. In contrast, the {220} and {222} reflections show that both phases yield at stresses higher than the bulk. For these orientations, the γ' phase yields first, leading to a steep increase in lattice strain in the γ phase as it takes on the load from the γ' phase. The {222} reflection exhibits the larger γ elastic modulus at 193, and 276 GPa for γ' in the {311} reflection. It is important to clarify that the stiffness/modulus reported here refers to the lattice-specific diffraction elastic constant (DEC), rather than the intrinsic bulk modulus. The DEC is an effective modulus governed by intergranular constraints and plastic anisotropy. Therefore, the apparent stiffening of specific grain families reflects a redistribution of load and constraint due to this change in slip activity, rather than a physical stiffening of the crystal lattice.

B. *Alloy B at 600 °C*

Figures 5(d) through (f) shows that for Alloy B at 600 °C, the load partitioning behavior is distinct. Unlike Alloy A, the γ' phase is the stiffest phase across the {200}, {311}, and {331} reflections, measuring at 291 GPa in the latter. The γ' phase yields at a stress lower than the bulk yield strength for all three reflections, ranging from 151 to 467 MPa, with a significant increase in lattice strain in the plastic region for the {200} orientation. Load transfer to the γ' phase occurs at approximately 100 MPa in the {200} reflection and 300 MPa in the {311} reflection, with the γ phase eventually taking on the load at higher stresses.

C. *Alloy C at 800 °C*

For Alloy C at 800 °C, Figures 5(g) through (i), the γ' phase is stiffer than the γ phase in the {220} and {311} reflections, at 134 and 156 GPa, respectively. While load transfer is not easily observed in the {200} reflection, it occurs at approximately 200 MPa in the {220} and 400 MPa in the {311} reflections. A greater accumulation of lattice strain in the plastic region is observed in the γ' phase compared to the γ phase, a consistent trend across all alloys. The yield of both γ and γ' phases in the {311} reflection occurs shortly before the bulk alloy yield at 557 MPa.

V. EFFECTS OF TEMPERATURE

A. *Alloy A – {200} and {220}*

A clear temperature-dependent shift in load partitioning is observed for Alloy A in both the {200} and {220} reflections, Figures 6(a) through (f). For the {200} reflection, Figures 6(a) through (c), the elastic moduli of the γ and γ' phases are similar at 600 °C at 114 and 115 GPa, respectively. However, γ becomes the stiffer phase at 700 °C to 800 °C, reaching 178 GPa at 700 °C. At 600 °C, the γ phase yields first, followed shortly by the γ' phase, with both yielding near the bulk strength. As temperature increases to 700 °C, the elastic moduli for both phases increase, and they continue to yield near the bulk value. At 800 °C, however, both phases show a decrease in elastic modulus, and their yield points are significantly lower than the bulk yield point, with the γ' phase yielding first at approximately 300 MPa.

A different trend is seen in the {220} reflection, Figures 6(d) through (f). Here, the γ' phase is significantly stiffer at 306 GPa, almost double that of γ at 600 °C. This behavior inverts at 700 °C and 800 °C, where the γ phase becomes stiffer. The γ' phase's elastic modulus decreases from 600 °C to 700 °C and then remains stable around 150 GPa, while its yield strength increases between these two temperatures before dropping significantly at 800 °C below 500 MPa. The γ' phase yields at a higher stress than the bulk at 600 °C and 700 °C but below the bulk at 800 °C. The γ phase follows a similar trend, yielding near or above the bulk strength at 600 °C and 700 °C, and below it at 800 °C.

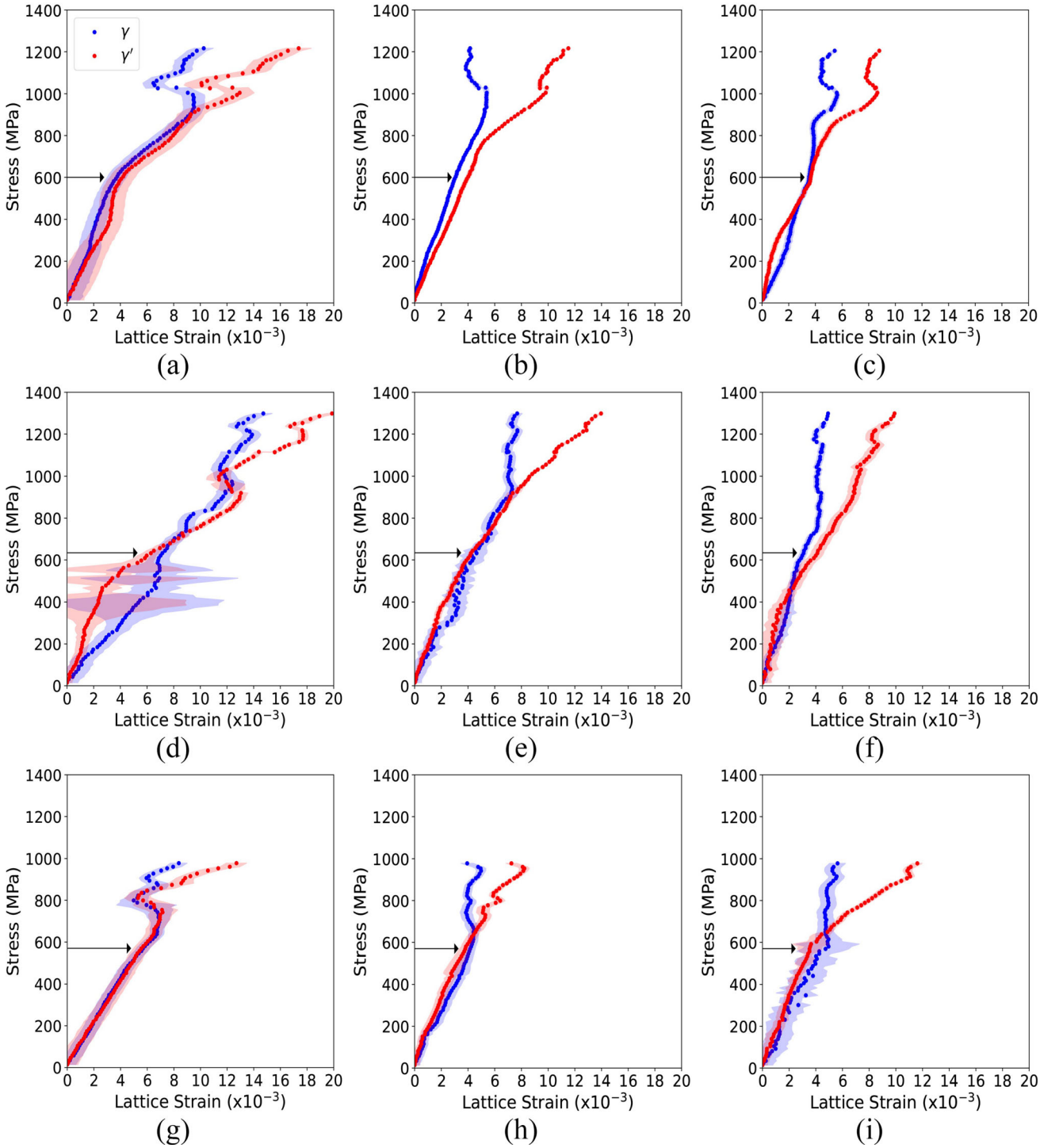

Fig. 5—Tensile behavior of the γ and γ' phases in three alloys at elevated temperatures, shown across various crystallographic reflections in (*a*) through (*c*) Alloy A at 700 °C:{200}, {220}, and {222} reflections, (*d*) through (*f*) Alloy B at 600 °C: {200}, {311}, and {331} reflections, (*g*) through (*i*) Alloy C at 800 °C: {200}, {220}, and {311} reflections, respectively. Arrows indicate the bulk alloy yield point for each alloy at its respective temperature. Numerical (Table S1) and graphical (Figures S2-3) summaries are provided in the electronic supplementary material.

B. *Alloy C – {220}*

In the {220} reflection for Alloy C, Figures 6(g) through (i), the γ' stiffness increases from 600 °C to 266 GPa at 700 °C before decreasing at 800 °C to 134 GPa, while the γ elastic modulus decreases continuously with temperature. A notable shift in load partitioning occurs at 700 °C, where the γ' phase becomes the stiffer phase and maintains this trend at 800 °C. The γ phase reaches its maximum yield

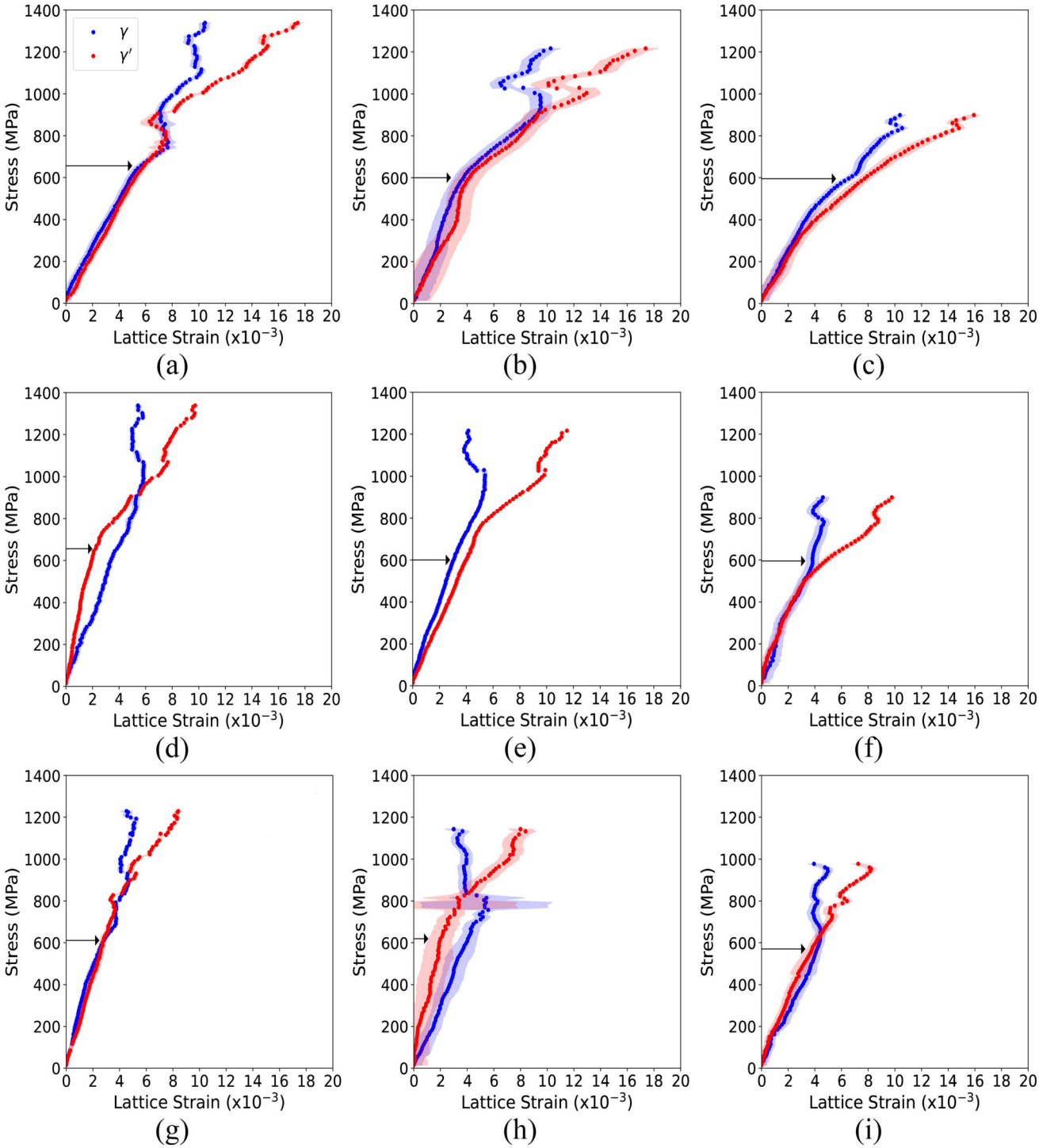

Fig. 6—Tensile behavior of the γ and γ' phases as a function of increasing temperature is shown across selected crystallographic reflections and alloys in (*a*) through (*c*) Alloy A in the {200} reflection, (*d*) through (*f*) Alloy A in the {220}, (*g*) through (*i*) Alloy C in the {220} reflection at 600 °C, 700 °C, and 800 °C (left–right), respectively. Arrows indicate the bulk alloy yield point for each alloy at its respective temperature. Numerical (Table S1) and graphical (Figures S2-3) summaries are provided in the electronic supplementary material.

strength at 700 °C, and in contrast to 600 °C where it yields just before the bulk, both phases yield after the bulk at 700 °C and 800 °C. Load transfer to the γ' phase begins immediately at 700 °C, while at 800 °C, it occurs at approximately 200 MPa.

VI. EFFECTS OF COMPOSITION

Varying the Ti:Ta ratio has a profound impact on the load partitioning behavior, with distinct trends observed across different temperatures and crystallographic orientations, Figure 7. In the {311} reflection (Figures 7(a) through (f)), the γ' phase is consistently the stiffest phase

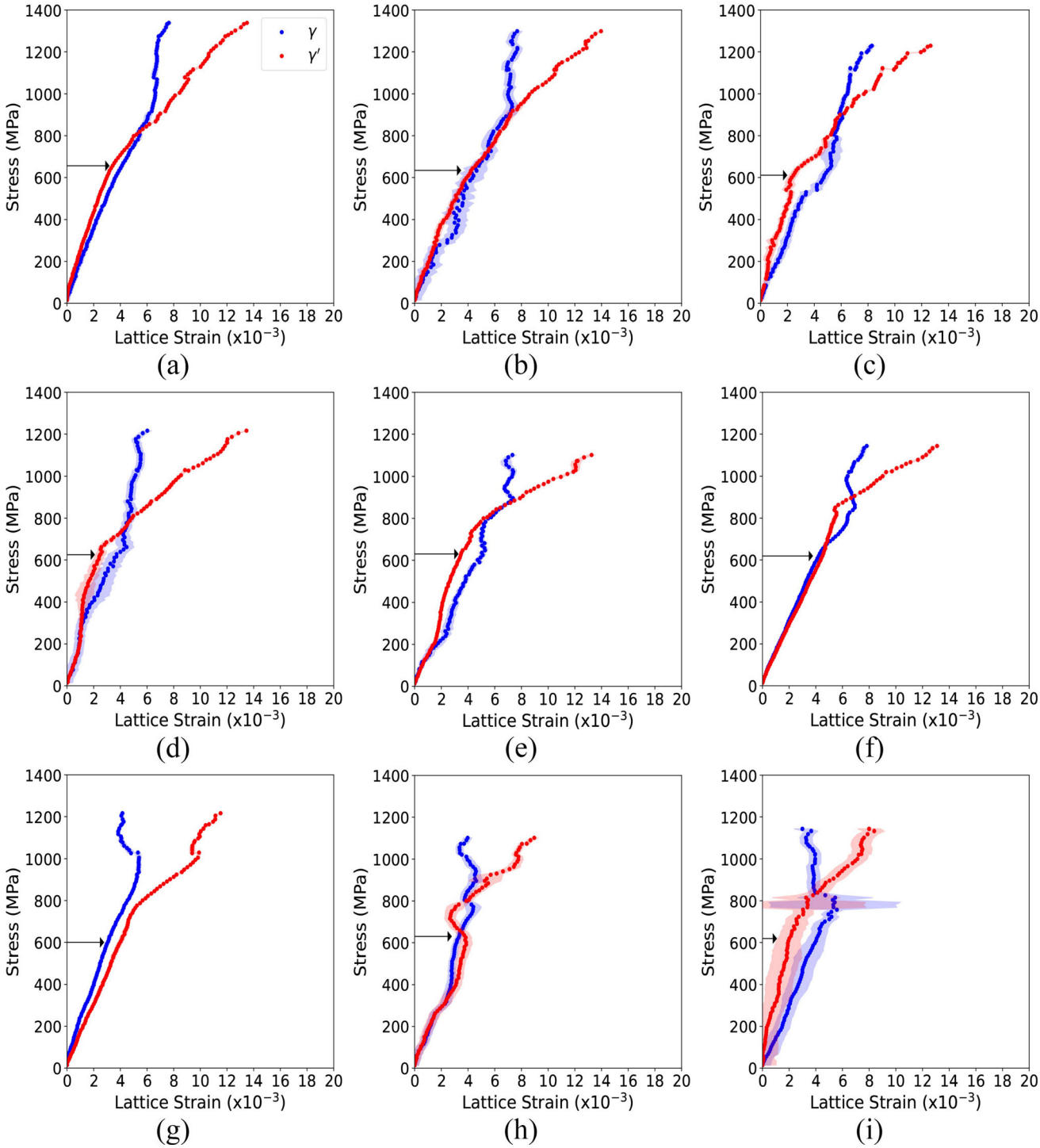

Fig. 7—Tensile behavior of the γ and γ' phases as a function of increasing Ti:Ta content in Alloys A, B, and C (left–right), shown across selected crystallographic reflections and temperatures in (*a*) through (*c*) {311} reflection at 600 °C, (*d*) through (*f*) {311} reflection at 700 °C, (*g*) through (*i*) {220} reflection at 700 °C, respectively. Arrows indicate the bulk alloy yield point for each alloy at its respective temperature. Numerical (Table S1) and graphical (Figures S2-3) summaries are provided in the electronic supplementary material.

across all three alloys at both 600 °C and 700 °C. At 600 °C, Alloy C shows the highest elastic modulus for the γ' phase at 225 GPa. This suggests that the higher Ti:Ta ratio strengthens the γ' phase. At 600 °C, Figures 7(a) through (c), the γ phase in Alloy A yields above the bulk strength at ~ 920 MPa, while in Alloys B and C, both phases yield at or near the bulk. The onset of load transfer from the γ to the γ' phase occurs for all alloys, but notably, this occurs at a lower stress level for Alloy C. Continuing the trend at 700 °C, Figures 7(d) through (f), the strength of the γ' phase progressively

increases from Alloy A to C, while the γ phase yields at a similar point for all alloys.

In the {220} reflection at 700 °C, Figures 7(g) through (i), a notable stiffness inversion is observed: the γ phase is stiffer in Alloys A and B at 166 and 176 GPa, respectively, while the γ' phase becomes the more dominant load-bearer in Alloy C at 266 GPa. This finding highlights a critical effect of elemental partitioning, where the higher Ti concentration in Alloy C likely partitions to the γ' phase, significantly affecting the micromechanics of that phase compared to the two alloys with comparatively lower Ti (but higher Ta) concentrations. This is further supported by the yield behavior, as the γ' yield strength increases from Alloy B to Alloy C.

VII. DISCUSSION

The focal point of this work is the direct link between the Ti:Ta ratio, load partitioning, and the resulting macroscopic bulk strength of the alloys as a function of temperature. The *in situ* diffraction data provide a mechanistic basis for the non-monotonic trend observed in the bulk strength, as the macroscopic response is the sum of the complex, phase-specific deformation mechanisms at the microstructural level.

It is important to contextualize these micromechanical observations against the initial microstructure. As detailed in the results section, the grain size was statistically equivalent across all three alloys (approx. 30 to 38 μm). Consequently, the variations in load partitioning and bulk strength observed herein cannot be attributed to Hall-Petch strengthening or grain size effects. However, the precipitate distribution did vary; Alloy C exhibited the highest secondary γ' volume fraction (53.6 pct). While the difference is modest relative to Alloys A and B (~ 48 to 50 pct), a higher volume fraction of the strengthening phase generally increases the geometric constraint on the γ matrix. This constraint can facilitate more efficient load transfer to the γ' precipitates[2] potentially amplifying the stiffness inversion effects driven by the compositional changes in the Ti:Ta ratio.

The *in situ* diffraction data demonstrate a strong correlation between crystallographic orientation and the onset of plastic deformation, a well-documented phenomenon in polycrystalline materials due to their inherent anisotropy and varying CRSS among grain families.[13, 26] In softer orientations, such as the {200} family, load transfer between the γ and γ' phases begins at relatively low applied stresses, with both phases yielding close to the bulk yield strength. This is in contrast to the stiffer {220} and {311} orientations, which exhibit a more nuanced, phase-specific behavior, with the γ' phase frequently being stiffer and yielding at significantly higher stress levels. For example, in Alloy B at 600 °C, load transfer begins at approximately 100 MPa in the {200} reflection, but not until 300 MPa in the {311} reflection. This behavior confirms that the yielding of grains in these 'soft' orientations effectively governs the macroscopic yield strength, as harder orientations (*e.g.*, {220}) remain elastic at this stress level. Furthermore, this finding is consistent with literature, as studies on CM247LC[3, 20] have also shown an orientation-dependent elastic response, with the γ' phase generally being stiffer than the γ phase, particularly in {110}-type grains. A neutron diffraction study on Waspaloy[13] similarly revealed significant residual microstrains and grain anisotropy, influencing the lattice strain behavior. The disproportionately high load carried by the γ' phase across all alloys and orientations confirms its role as the primary strengthening phase, and its varying response highlights how small compositional changes can have a large impact on its load-bearing capacity.

The *in situ* diffraction data also reveal a complex, temperature-dependent load partitioning behavior. A key finding is the stiffness inversion between the phases, particularly evident in the {220} reflection. For Alloy A, the stiffer γ' phase at 600 °C gives way to a stiffer γ phase at 700 °C and 800 °C. In contrast, the γ' phase in Alloy C becomes and remains the stiffer component from 700 °C onwards. This thermally driven shift is consistent with findings from Daymond *et al.*[21] and Preuss *et al.*,[16] who attributed similar stiffness inversions in U720Li and RR1000 to a change in the active slip system from {111} to {100} planes. It is important to clarify that the 'stiffness' reported here refers to the lattice-specific diffraction elastic constant, rather than the intrinsic bulk modulus. While intrinsic bond strength decreases with temperature, the DEC is an effective modulus governed by intergranular constraints and plastic anisotropy; thus, the observed stiffening reflects a redistribution of load due to this change in slip activity.

Furthermore, temperature controls the initiation of load transfer to the stiffer phase; in Alloy C, load transfer starts immediately at 700 °C but is delayed until 200 MPa at 800 °C. This indicates that while the γ' phase is the primary load-bearer at higher temperatures for some compositions, the onset of its load-carrying function is sensitive to the specific temperature and alloy chemistry. In addition, while U720Li and most other alloys in the literature possess relatively low Co contents compared to the alloys studied here, the consistency of the observed trends, both the stiffness inversion and the Ti/Ta influence on load partitioning, across these varying Co levels suggests that the mechanisms described herein are likely robust across the superalloy compositional space.

Varying the Ti:Ta ratio significantly influences the load partitioning behavior, which directly affects the relative stiffness and strength of both the γ and γ' phases. As the Ti:Ta ratio increases, the γ' phase becomes progressively stiffer, as evidenced by its high elastic modulus in Alloy C, particularly in the {311} reflection at both 600 °C and 700 °C. This stiffness mismatch facilitates efficient load transfer, allowing the γ' phase to attract a greater proportion of the applied stress, with the onset of load transfer from the γ matrix occurring at a notably lower stress level for Alloy C. A stiffness inversion is also observed in the {220} reflection at 700 °C, where the γ' phase in Alloy C effectively shields

the matrix, unlike in Alloys A and B. While this elastic mismatch drives load partitioning, the capacity of the γ' phase to sustain these high internal stresses without yielding is attributed to the APBE. Calculated APBEs were found to be highest in Alloy C, followed by Alloy A and then Alloy B, with energies larger in the {111} plane than the {100} plane, Figure 8. While literature often reports an increase in APBE with rising Ti content,[9, 27] the lack of a direct linear correlation in this study suggests that APBE magnitude is likely governed by a synergistic interaction between Ti and Ta, rather than Ti concentration alone. Other microstructural characteristics, such as precipitate size or complex elemental partitioning between the γ matrix and the multimodal γ' precipitates, may also contribute to this non-monotonic trend. Additionally, the interplay between Ti and Ta will also affect MC carbide formation, which may further impact mechanical performance. However, the distinct stiffness inversion observed in Alloy C remains consistent with its high intrinsic APBE. It is noted that while the nominal Al content was fixed at 6.4 at. pct, the actual composition of Alloys A and C exhibited a deviation of approximately 0.5 at. pct (Table I). Although this compositional shift is acknowledged, it is unlikely to significantly influence the load partitioning behavior observed. Research by Crudden *et al.*[24] has established that while Al primarily controls the volume fraction of the γ' phase, the intrinsic strengthening, specifically the APBE, is predominantly governed by the concentrations of Ti, Ta, and Nb. Consequently, the stiffening behavior of Alloy C is driven by the high intrinsic APBE and lattice parameters imparted by Ti and Ta, rather than minor fluctuations in precipitate fraction. Furthermore, to ensure rigorous correlation, the theoretical APBE calculations presented herein were performed using the actual measured compositions rather than the nominal values, thereby fully accounting for the specific chemistry of the tested alloys. However, a note of caution is added that while the actual compositions were used, there may still be errors in the calculation, particularly as the APBE energy requires accurate γ' compositions. This highlights the critical role that composition plays in determining deformation behavior, as demonstrated by Goodfellow *et al.*,[28] who found that similar bulk yield strengths in different alloys did not guarantee similar load partitioning behavior.

Lattice misfit was found to influence load partitioning behavior, with the higher misfit of Alloy A (due to its higher Ta content) correlating with different load transfer dynamics compared to the other alloys. This supports the findings of Goodfellow *et al.*,[2] who reported that larger misfit magnitudes, regardless of whether positive or negative, correlated with increased load partitioning. While a simple relationship between misfit and bulk yield strength was not identified in this study, the results confirm that misfit is a critical factor influencing the micro-mechanical response of the individual phases. Additionally, the decrease in misfit at higher temperatures, particularly for Alloy A, highlights the importance of understanding high-temperature misfit, which is a key parameter for predicting and controlling γ' coarsening kinetics.

A comparison of the *in situ* load partitioning behavior to the bulk strength results reveals that the microscopic, phase-specific deformation mechanisms directly explain the more complex macroscopic mechanical response. The non-monotonic bulk strength trend is a direct result of the shifting load-bearing responsibilities between the γ and γ' phases. For instance, the significant decline in Alloy A's bulk strength at higher temperatures is explained by the *in situ* data showing its γ' phase losing relative stiffness, thus becoming less effective at carrying the applied load. Conversely, the improved bulk strength of Alloy C at 700 °C is directly correlated with the observed stiffness inversion in the {220} reflection, where its γ' phase becomes the dominant and more effective load-bearer. However, at 800 °C, Alloy C exhibits a sharp decline in yield strength, which correlates with the substantial decrease in γ' stiffness observed in Figure 6(i). In contrast, Alloy B demonstrates the most consistent yield strength across the temperature

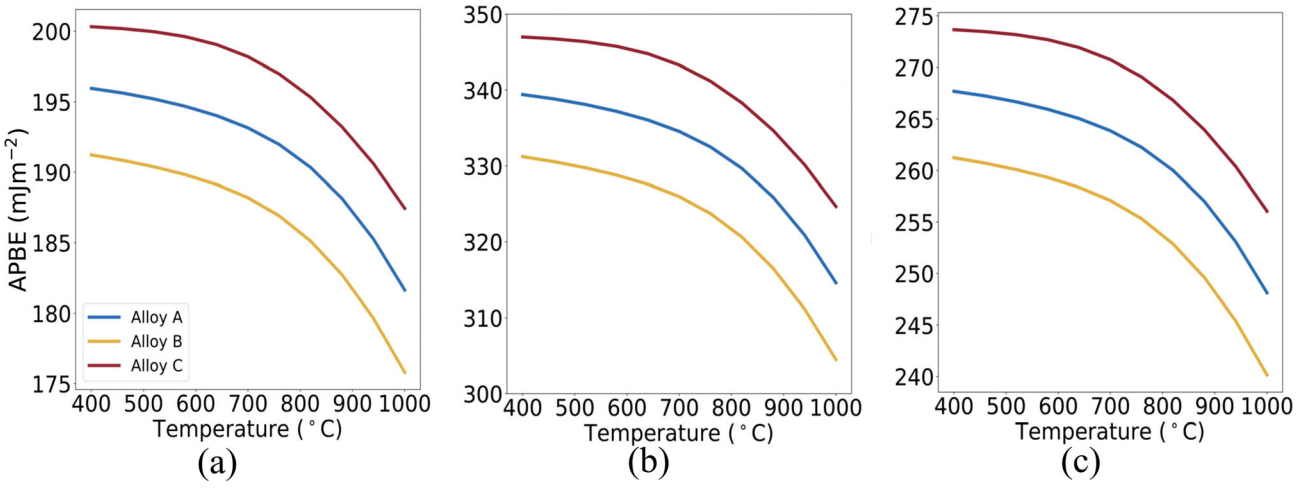

Fig. 8—The APBEs of Alloys A and B were calculated in Thermo-Calc, using their actual compositions. The Anti-phase Boundary Property Model Calculator was applied for the (*a*) {100}, (*b*) {111} slip systems, and (*c*) the average between {100} and {111}.

range, suggesting that a balanced Ti:Ta ratio offers greater stability at the highest temperatures. To fully elucidate the drivers of these stability differences, further investigation into the precise elemental partitioning of Ti and Ta between the matrix and precipitate phases is required. Therefore, the *in situ* diffraction data successfully provide a mechanistic basis for the bulk strength observations.

Beyond explaining the observed bulk properties, the findings of this study provide critical guidance for future alloy design. By demonstrating that the Ti:Ta ratio can be used to precisely tune the load partitioning behavior between the γ and γ' phases, this work provides further evidence for the optimization of the Ti:Ta ratio for mechanical performance. Instead of a trial-and-error approach to macroscopic properties, targeted compositional adjustments to control the micromechanical deformation of the alloy can be utilized. The data suggest that a balanced Ti:Ta ratio can lead to a more stable yield point across a range of operating temperatures, while a higher Ti:Ta ratio can be used to specifically enhance high-temperature strength. This mechanistic understanding allows for the rational design of superalloys with properties tailored for specific service conditions, moving the field toward a more predictive and efficient alloying process.

VIII. CONCLUSION

This study sought to explore the influence of Ti and Ta co-additions on the thermomechanical properties of high Co-containing, powder-processed polycrystalline Ni-based superalloys. *In situ* synchrotron X-ray diffraction results revealed that the Ti:Ta ratio fundamentally controls the load partitioning between the γ and γ' phases. A direct relationship where a higher Ti:Ta ratio, as seen in Alloy C, resulted in a stiffer γ' phase, which became the primary load-bearer at 700 °C, was observed. This was mechanistically explained by the high intrinsic APBE associated with the specific Ti:Ta synergy.

The *in situ* synchrotron X-ray diffraction data also explain the complex temperature-dependent and orientation-specific mechanical behavior of these alloys, where softer orientations, such as grains in the {200} family, yield at lower stresses while stiffer orientations like {220} and {311} families show a more nuanced response with the γ' phase carrying a higher load, providing a direct link between the microstructural response and the macroscopic bulk strength. Ultimately, this work provides a valuable framework for designing next-generation superalloys with properties precisely tailored for demanding, high-temperature, structural applications.

ACKNOWLEDGMENTS

This work was supported by Rolls-Royce plc and the EPSRC [EP/S022635/1]. K.A. Christofidou also acknowledges from EP/R00661X/1 and EP/S019367/1. Data were collected at the European Synchrotron Radiation Facility (ESRF) [ME1344]. The authors gratefully acknowledge ETMT and LIPRAS assistance from Dr. H.T. Pang and Dr G. Esteves, respectively.

DATA AVAILABILITY

The raw and analyzed data are provided here: https://doi.org/10.15131/shef.data.31132747.

CONFLICT OF INTEREST

On behalf of all authors, the corresponding author states that there is no conflict of interest.

SUPPLEMENTARY INFORMATION

The online version contains supplementary material available at https://doi.org/10.1007/s11661-026-08142-x.

REFERENCES

1. D. Dye, J. Coakley, V.A. Vorontsov, H.J. Stone, and R.B. Rogge: *Scripta Mater.*, 2009, vol. 61(2), pp. 109–12.
2. A.J. Goodfellow, J. Kelleher, N.G. Jones, D. Dye, M.C. Hardy, and H.J. Stone: *Acta Mater.*, 2019, vol. 176, pp. 318–29.
3. J. Coakley, and D. Dye: *Scripta Mater.*, 2012, vol. 67(5), pp. 435–38.
4. J.R. Davis: *Alloying : understanding the basics*, 1st ed. ASM International, Materials Park, 2001.
5. M.T. Jovanović: *Metall. Mater. Eng.*, 2016, vol. 22(3), pp. 205–20.
6. C. Chu, Q. Guo, R. Ding, and Y. Liu: *Mater. Charact.*, 2023, vol. 199, 112841.
7. Z.-Y. Meng, G.-C. Sun, and M.-L. Li: *Superalloys 1984*, Seven Springs, Pennsylvania, 1984.

8. S.C.H. Llewelyn, L.R. Owen, H.Y. Playford, N.G. Jones, D. Dye, M.C. Hardy, and H.J. Stone: *J. Alloys Compd.*, 2023, vol. 937, 168253.
9. S.C.H. Llewelyn, K.A. Christofidou, V.J. Araullo-Peters, N.G. Jones, M.C. Hardy, E.A. Marquis, and H.J. Stone: *Acta Mater.*, 2017, vol. 131, pp. 296–304.
10. N.G. Jones, K.A. Christofidou, P.M. Mignanelli, J.P. Mishull, M.C. Hardy, and H.J. Stone: *Mater. Sci. Technol.*, 2014, vol. 30(15), pp. 1853–61.
11. C.Y. Cui, Y. Gu, D. Ping, and H. Harada: *Mater. Trans.*, 2008, vol. 49(3), pp. 424–27.
12. C.Y. Cui, Y.F. Gu, D. Ping, and H. Harada: *Metall. and Mater. Trans. A.*, 2009, vol. 40(2), pp. 282–91.
13. H.J. Stone, T.M. Holden, and R.C. Reed: *Acta Mater.*, 1999, vol. 47(17), pp. 4435–48.
14. G.E. Bacon and K. Lonsdale: *Rep. Prog. Phys.*, 1953, vol. 16(1), p. 1.
15. T. Ungár: *Scripta Mater.*, 2004, vol. 51(8), pp. 777–81.
16. M. Preuss, J. Fonseca, B. Grant, E. Knoche, R.J. Moat, and M. Daymond: *The Effect of γ' Particle Size on the Deformation Mechanism in an Advanced Polycrystalline Nickel-Base Superalloy*. Proceedings of the International Symposium on Superalloys. 2008.
17. M.C. Hardy, H.J. Stone, S. Neumeier, N.G. Jones, and K. Christofidou: *Nickel Alloy*, P. United States, Editor, 2018.
18. M.C. Hardy, H.J. Stone, S. Neumeier, N.G. Jones, and K. Christofidou: *A Nickel Alloy*, O. European Patent, Editor, 2017.
19. G. Esteves, K. Ramos, C. Fancher, and J. Jones: *LIPRAS: Line-Profile Analysis Software*, 2017.
20. S. Ma, P. Rangaswamy, and B.S. Majumdar: *Scripta Mater.*, 2003, vol. 48(5), pp. 525–30.
21. M.R. Daymond, M. Preuss, and B. Clausen: *Acta Mater.*, 2007, vol. 55(9), pp. 3089–3102.
22. A. Miodownik, N. Saunders, P. Nash, and B. Sundman: *Applications of Thermodynamics in the Synthesis and Processing of Materials,* TMS, 1995.
23. N. Saunders, M. Fahrmann, and C.J. Small: *The Application of Calphad Calculations to Ni-Based Superalloys*, TMS, 2000.
24. D.J. Crudden, A. Mottura, N. Warnken, B. Raeisinia, and R.C. Reed: *Acta Mater.*, 2014, vol. 75, pp. 356–70.
25. Y.-X. Liu and Y.C. Lin: *High Temp. Mater. Process.*, 2018, vol. 37(9–10), pp. 849–56.
26. D. Dye, H.J. Stone, and R.C. Reed: *Curr. Opin. Solid State Mater. Sci.*, 2001, vol. 5(1), pp. 31–37.
27. M. Dodaran, A.H. Ettefagh, S.M. Guo, M.M., Khonsari, W.J. Meng, N. Shamsaei, and S. Shao: *Intermetallics*, 2020, vol. 117, p. 106670.
28. A.J. Goodfellow, L.R. Owen, K.A. Christofidou, J. Kelleher, M.C. Hardy, and H.J. Stone: *Metals*, 2019, vol. 9(6), p. 700.